ECS Journal of Solid State
Science and Technology

ACCEPTED MANUSCRIPT

Role of Fe (x=0-0.15) Substitution on Structural, Magnetic, and Transport Properties of the $La_{0.7}Sr_{0.3}Fe_xMn_{1-x}O_3$ System

To cite this article before publication: Kumar Navin *et al* 2021 *ECS J. Solid State Sci. Technol.* in press https://doi.org/10.1149/2162-8777/ac10b5

Role of Fe (x=0-0.15) Substitution on Structural, Magnetic, and Transport Properties of the $La_{0.7}Sr_{0.3}Fe_xMn_{1-x}O_3$ System

Journal:	*ECS Journal of Solid State Science and Technology*
Manuscript ID	JSS-101309.R1
Manuscript Type:	Research Paper
Date Submitted by the Author:	15-Jun-2021
Complete List of Authors:	Navin, Kumar; Maulana Azad National Institute of Technology, Nanoscience and Engineering Center, Department of Physics Subohi, Oroosa; Visvesvaraya National Institute of Technology, Department of Physics Ball, Richard; University of Bath, BRE Centre for Innovative Construction Materials, Department of Architecture and Civil Engineering Kurchania, Rajnish; Maulana Azad National Institute of Technology, Department of Physics
Keywords:	B-site doping, Nanoscale materials, Trasport properties, Magnetoresistance

Role of Fe (x=0-0.15) Substitution on Structural, Magnetic, and Transport Properties of the $La_{0.7}Sr_{0.3}Fe_xMn_{1-x}O_3$ System

Kumar Navin,[1] Oroosa Subohi,[2] Richard J. Ball,[3] and Rajnish Kurchania[1, z]

[1]Functional Nanomaterials Laboratory, Department of Physics, Maulana Azad National Institute of Technology (MANIT), Bhopal-462003, India

[2]Department of Physics, Visvesvaraya National Institute of Technology (VNIT), Nagpur, Maharashtra-440010, India

[3]BRE Centre for Innovative Construction Materials, Department of Architecture and Civil Engineering, University of Bath, Claverton Down, Bath BA2 7AY, UK

[z]E-mail: rkurchania@gmail.com

This paper investigates the effect of Fe substitution on the structural, magnetic and transport properties of the $La_{0.7}Sr_{0.3}Mn_xFe_{1-x}O_3$ (LSMO) system where x ranged between 0 and 0.15. Samples were prepared using a non-aqueous sol-gel synthesis method. Structural and chemical analysis confirmed the Fe^{3+} substitution at Mn^{3+} sites without any impurity phase resulted in a small change in structural parameters of the LSMO. The change in magnetic behavior and Curie temperature of the Fe-doped LSMO is explained through competitive exchange interactions developed in the system. The temperature-dependent resistivity demonstrated that the resistivity of the samples increased with Fe concentration due to different conduction mechanisms related to the ferromagnetic-metallic and paramagnetic-insulating regions. The magneto-transport measurement showed significant improvement in the magnetoresistance due to Fe doping at Mn site, which was attributed to enhancement of the spin-glass phase in Fe doped LSMO system. The reduction in magnetoresistance for higher Fe concentration is explained with the help of percolation threshold mechanism.

1. Introduction

The perovskite manganite (ABO_3: A=trivalent rare earth, and B=transition metal) is an important compound with interesting magnetic and transport properties and several promising applications. Among these systems, $La_{0.7}Sr_{0.3}MnO_3$ (LSMO) is one of the most important members of the perovskite manganite family due to its interesting properties such as colossal magnetoresistance (CMR), metal-insulator transition, ferromagnetic-paramagnetic transition, excellent catalytic properties that make it suitable for application in magnetic field sensors, biomedical devices, EMI shielding, fuel cell technology, and electrochemical charge storage applications[1-5]. The magnetic and transport behavior of LSMO is explained in terms of the exchange interaction (double exchange and superexchange) between Mn ions through oxygen ions[6]. Different methods for improving the magnetic, transport, and catalytic properties of the LSMO have been reported, including different synthesis methods, varying particle size, strain engineering, doping at A- and B-sites with other rare-earth and transition metal ions, and tuning the nature of the grain boundary[7-12].

Among these methods, doping at A- and B-sites in the LSMO system is an important field of research because it changes the structure and charge transport mechanism of the system. There are different reports available on the study of the substitution of La^{3+} (A-site) with other rare-earth ions (Y, Sm, Ce, Bi, Gd, and Nd etc.) in addition to the Sr on the magnetic and transport parameters of LSMO[12-17]. Doping at the A-site directly affects the Mn-O-Mn bond angle which modifies the magnetic and transport properties. The doping at the A-site results in improvement in magnetocaloric effect, temperature coefficient of resistance (TCR), and magnetoresistance of the LSMO[17]. Furthermore, the doping by other transition metals at the B-site is also of interest as it directly affects the charge transport mechanism involved in LSMO. The substitution of the transition metal at Mn sites disrupts the Mn^{3+}-O^{2-}-Mn^{4+} chain leading to the alternation of the

Mn^{3+}/Mn^{4+} ratio. Previous research has investigated doping with other transition metals including Cu, Fe, Ni, Co, and Ru at the Mn site in the LSMO system[11, 18-24]. Substitution at the Mn-site with transition metals has been reported to have a significant effect on the magnetic and transport behavior of LSMO[18]. The resistivity of the sample increases with doping at the Mn-site along with a suppression of the magnetic transition and metal-insulator transition temperature of the system[20]. Doping at the B-site by Co, Ni and Fe have also been reported to have weakened the magnetic behavior of LSMO due to a decrease in the double exchange interaction between Mn ions[11, 18, 20]. The low field magnetoresistance (LFMR) shows significant improvement due to the doping of other transition metals at the Mn site. The study of the effect of Fe doping at the B-site in LSMO is particularly important from the fundamental understanding of its properties and applications due to nearly similar ionic radii and electronic configurations of Fe and Mn [$Fe^{3+}(t_{2g\uparrow}^3 e_{g\uparrow}^2)$ = 0.645Å, $Mn^{3+}(t_{2g\uparrow}^3 e_{g\uparrow}^1)$ = 0.645Å, $Mn^{4+}(t_{2g\uparrow}^3 e_{g\uparrow}^0)$ = 0.53Å] ions. It has been observed that the magnetoresistance increases for the lower doping level of Fe at the Mn site, due to the formation of the spin-glass phase in the system. Therefore, a systematic study of the effect of Fe doping at the Mn site on the magnetic and transport properties of LSMO becomes essential.

In this work, Fe-doped LSMO [$La_{0.7}Sr_{0.3}Mn_{1-x}Fe_xO_3$; x=0, 0.03, 0.06, 0.09, 0.12, and 0.15] has been synthesized using the non-aqueous sol-gel method. The structural, magnetic, transport and magneto-transport behavior of the Fe-doped LSMO have been systematically investigated. The transport behavior of the $La_{0.7}Sr_{0.3}Mn_{1-x}Fe_xO_3$ system has been explained with different conduction processes involved in different temperature regions.

2.Experimental details

(a) Synthesis method

$La_{0.7}Sr_{0.3}Mn_{1-x}Fe_xO_3$ [x=0 (LSMO), 0.03 (LF3), 0.06 (LF6), 0.09 (LF9), 0.12 (LF12), and 0.15 (LF15)] samples are synthesized using a sol-gel method. Fig.1 shows the flow diagram for synthesis of Fe-doped LSMO samples. The stoichiometric amount of metal acetate precursors was mixed with ethylene glycol and the solution obtained was then refluxed at 120ºC for 12 h. The obtained gel was dried at 120ºC to remove the solvent. The resulting brown colored powder was ground well and calcined at 600ºC to form the Fe-doped LSMO. The powder obtained was then pressed to form a pellet which was subsequently sintered at 800°C for 4 h.

(b) Characterization

X-ray diffraction (XRD) (Bruker-D8 Advanced, Cu-K_α radiation λ=1.54Å), Field emission scanning electron microscopy (Zeiss Ultra FESEM), and Transmission electron microscopy (TEM CM 200) was used to structurally analyze the samples. The structural parameters of the XRD pattern were determined by Rietveld refinement by using the FULLPROF computer program[25]. Compositional and chemical analysis of the samples was performed using energy dispersive spectroscopy (EDAX) and X-ray photoelectron spectroscopy (XPS). The magnetization with temperature (M-T) and isotherm magnetization (M-H) of the samples was measured using SQUID-VSM (Quantum design Inc.). The isotherm magnetization was measured at 10 K and 300 K in a magnetic field of -4 T to 4 T. The temperature-dependent resistivity (ρ-T) was measured using the four-probe technique in an MPMS system (Quantum design Inc.) in the temperature range of 10 K to 300 K. The magnetoresistance measurement was performed as a function of magnetic field at 10 K and 300 K.

3. Results and discussion

3.1 Structural analysis

XRD patterns of the Fe-doped (x=0, 0.03, 0.06, 0.09, 0.12, 0.15) LSMO samples are shown in Fig.2. The peaks of the diffraction patterns are indexed with the rhombohedral structure ($R\bar{3}c$, JCPDS-50-0308) which confirms the single-phase nature of the as prepared perovskite samples without any peaks relating to impurities. To clarify the effect of Fe doping on the XRD pattern, the diffraction patterns were enlarged in the range of 2θ=32-33.5º (Inset of Fig.2). A very small peak shift towards the higher angle side of the diffraction pattern with an increase in the doping concentration of Fe ions is clearly visible, indicating a small change in the structural parameters of the sample due to Fe doping at the Mn site. The structural parameters were obtained from the refinement of the XRD pattern of the Fe-doped LSMO samples. Fig.3 (a) shows the refined XRD data of the LSMO and LF-15 samples and structural parameters are summarized in the Table-1. The crystal structure observed from the structural parameters are shown in Fig.3 (b). It has been reported that the doping of Fe at B-site in LSMO results in the replacement of Mn^{3+} ion by Fe^{3+} [20]. Thus, a negligible change in lattice parameter and cell volume is expected because of the similar ionic radii of the Mn^{3+} and Fe^{3+} (0.645Å). However, a small change observed in the lattice parameters of the Fe doped samples is attributed to the formation of magnetic polarons[26]. The magnetic polaronic state results in the change in Mn-O bond length and thus results in the change in other structural parameters of the Fe doped LSMO samples.

The crystallite size of the Fe-doped samples as calculated from the Debye Scherrer method were 18.2nm, 15.9nm, 15.38nm, 15.64nm, 15.24nm, and 16.39nm for LSMO, LF3, LF6, LF9, LF12, and LF15 samples respectively. Thus, the crystallite size of the samples decreased with the increase in Fe concentration at the Mn site [Fig.3(c)]. The morphological and compositional

analysis of the LSMO and LF-15 are shown as FESEM and TEM micrographs in Fig.4(a-c). They clearly show that both samples have a spherical or ellipsoidal shape, and the particle size is reduced in the B-site doped LSMO. The average particle size was calculated as 35.5 nm and 19.4 nm for LSMO and LF-15 samples respectively. The energy dispersion spectroscopy was performed for the elemental analysis of the samples, as shown in Fig.4(a-c). It shows the presence of all the elements in the required elemental ratio in the sample. The elemental ratio obtained from the EDS measurement is shown in Fig.4 for LSMO and LF-15 samples, which is very close to the required stoichiometry of the sample.

2. X-ray photoelectron spectroscopy (XPS) analysis

The XPS measurement is used to determine the chemical nature of the LSMO and Fe-doped LSMO samples. The core-level XPS spectra of the LSMO, LF6, and LF-15 samples are shown in Fig.5. The survey spectrum of the LSMO, LF6 and LF15 is shown in Fig.5(a), which confirms the existence of all constituent elements (La, Sr, Mn, Fe, and O) in the sample. The enlarged spectrum of the Mn 2p, and Fe 2p is deconvoluted to examine chemical state and composition with the help of Voigt function with Shirley background.

Fig.5(b) shows the Mn 2p XPS core level spectra of the LSMO, LF6 and LF15 samples. The Mn 2p XPS spectra show two peaks related to the Mn $2p_{1/2}$ and Mn $2p_{3/2}$ due to spin-orbit splitting, which is deconvoluted using Mn^{3+}, Mn^{4+}, and satellite peaks[27]. The ratio of the Mn^{4+}/Mn^{3+} calculated for the LSMO and Fe doped LSMO samples showed an increase due to Fe doping [Fig.5(c)]. This confirmed the substitution of Fe ions at the Mn^{3+} sites. The core-level spectra of the Fe 2p is shown in Fig.5(d). The Fe 2p spectra is deconvoluted into Fe $2p_{3/2}$ (~ 711 eV), Fe $2p_{1/2}$ (~724 eV), and shake-up satellite peaks[28]. The Fe 2p spectra confirms the presence

of Fe in the +3 state within the sample, which agrees with previous studies of the Fe doped samples [29, 30].

3.3 Magnetic properties

Fig.6 shows M-H measurement of the Fe-doped LSMO samples at 10 K. The M-H plots clearly show the ferromagnetic behavior of Fe-doped LSMO, for $x \geq 0.09$ the M-H loop remains unsaturated up to a magnetic field of 4 T. The saturation magnetization (M_s) also decreases with Fe concentration at the Mn site as shown in Table-2 [Fig.7(a)]. The magnetic properties of the LSMO can be described with the help of a double exchange (DE) mechanism between Mn ions (Mn^{3+}-O^{2-}-Mn^{4+}). When the Mn ion is replaced by Fe (Fe^{3+}) the ratio of the Mn^{4+}/Mn^{3+} increases, which is confirmed by the XPS analysis. As a result, the long-range ferromagnetic order of the Mn^{3+}-O^{2-}-Mn^{4+} is disturbed and the resulting antiferromagnetic contribution (Mn^{3+}-O^{2-}-Mn^{3+}) increases leading to a decrease in the overall magnetization of the sample[26]. An increase in Fe concentration at the Mn-site weakens the DE interaction between Mn ions, as a result, M_s decreases with Fe doping. An increase in the coercivity of the sample with the doping concentration of Fe [Fig.6(a)] was also observed and is explained in terms of the pinning of the domain wall motion by Fe ions[18]. In addition, the blocking of the glass state generated by the random distribution of the Fe ion in the Mn network is also responsible for the higher coercivity observed in the samples[11].

The temperature-dependent magnetization (H=0.01 T) of the LSMO, LF6 and LF15 samples are shown in Fig.7(b). The bifurcation in the ZFC-FC curve is attributed to the spin-glass system or superparamagnetic nature of the system[31]. The spin-glass like behavior of LSMO nanoparticles has been reported due to the presence of spin disorder present in the system[9]. The

random distribution of Fe in the LSMO system increases the presence of the spin-glass phase. Bifurcation of the ZFC-FC curve also indicates pinning of the domain wall motion due to the spin -glass phase in the system. The increase in coercivity of the sample with Fe doping also confirms the enhanced role of spin-glass phase on the domain wall motion[18]. The ferromagnetic-paramagnetic transition (T_c) temperature of the LSMO, LF6, and LF15 samples are calculated as 352 K, 255 and 226 K, respectively. A drastic decrease in the T_c of Fe doped samples are due to the strong competition between the ferromagnetic double exchange mechanism and antiferromagnetic interaction. Therefore, the magnetic contribution of Fe doping at the Mn site is explained in terms of the increased antiferromagnetic state that weakens the ferromagnetic exchange interaction in the LSMO system.

3.4 Transport properties

The temperature-dependent resistivity of the Fe-doped LSMO sample in the temperature range of 10K-300K is shown in Fig.8. The results show that the resistivity of the samples is extremely sensitive to the extent of Fe substitution at the Mn site. Fig.9 shows that the resistivity increases and the transition temperature (T_{M-I}) decreases with Fe doping. The double exchange mechanism is used to explain the conduction of charge carriers in LSMO. In the case of the Fe-doped LSMO samples, Fe^{3+} ions replace the Mn ions and change the Mn^{3+}/ Mn^{4+} ratio weakening the double exchange mechanism that results in the decrease of the active sites available for charge carrier hopping[32]. The number of ferromagnetic clusters used for the conduction decreases and antiferromagnetic clusters increase with Fe doping. This results in the scattering of charge carriers and an increase in the overall resistivity of the sample[33]. Thus, the Fe substitution weakens the double exchange process that increases the resistivity of the sample and decreases the value of the transition temperature. In addition, it has been also reported that doping at B-site results in the

modification of the grain boundary region due to interdiffusion of the dopant atoms that result in the augmentation of the resistivity of the sample[34].

A different charge transport mechanism is used to explain the resistivity variation with temperature of the Fe-doped LSMO samples. In metallic regions ($T<T_{MI}$), the resistivity can be explained with the model given as $\rho = \rho_0 + \rho_2 T^2 + \rho_{4.5} T^{4.5}$, where, ρ_0 is related to the grain boundary scattering, $\rho_2 T^2$ is the electron-electron scattering, and $\rho_{4.5} T^5$ is electron-magnon scattering process[35, 36]. The parameters obtained from the resistivity fitting in the ferromagnetic metallic region are summarized in Table-3. For $T>T_{MI}$ (paramagnetic-semiconducting region), the resistivity of the sample decreases with increases in temperature. The resistivity in this region is explained with the adiabatic small polaron hopping (ASPH) model: $\rho = \rho_0 \exp(E_a/k_B T)$ for $T_{MI}< T > \theta_D/2$ range, where ρ_0 is residual resistivity, E_a is the activation energy, k_B is Boltzmann constant, and θ_D is the Debye temperature[37]. Resistivity is fitted with the ASPH model [ln(ρ/T) vs.1000/T], and the parameters obtained are summarized in Table-3. The activation energy (E_a) increases with Fe doping concentration at the B-site which indicates that electrons become localized with Fe doping and are unable to cross the potential barrier (E_a), which also results in an increase in the sample resistivity[26].

The temperature ($T_{MI}< T< \theta_D/2$) at which the resistivity diverged from linearity [in ln(ρ/T) vs.1000/T plot] is described with the VRH model: $\rho = \rho_0 \exp(T_0/T)^{1/4}$, where $T_0=16\alpha^3/k_B N(E_F)$, $N(E_F)$ is the density of states at Fermi level, $\alpha=2.22$ nm^{-1} [38]. The resistivity is fitted using the VRH model [ln(ρ) vs. $T^{-0.25}$] and parameters obtained are shown in Table-3. The value of T_o increases while $N(E_F)$ decreases with Fe doping which indicates an increase in the localization of charge carriers[39].

The field dependence magnetoresistance [$MR=(\rho_0-\rho_H)/\rho_0$] of the Fe doped LSMO samples at 10 K and 300 K are shown in Fig.10 (a). The MR is divided into the low field region (H< 0.5 T), and high field region (H>0.5 T) with respect to the different mechanisms involved. In the low field region, the sharp drop of resistivity due to the magnetic field is attributed to the spin polarized tunneling or scattering of the conduction electron. The high magnetic field region of the MR is explained in terms of the noncollinear structure near the grain boundary region. The MR behavior of the Fe doped LSMO is strongly dependent on the Fe doping concentration at Mn sites. The results obtained from the MR are summarized in Table-2 and variation of MR with Fe concentration is shown in Fig.10 (b). MR values, at 10 K with 0.5 T magnetic field, of 27.9%, 30.7 %, 32.1 %, 33.8 %, 23.12 %, and 19.8 % for the LSMO, LF3, LF6, LF9, LF12, and LF15 samples were obtained respectively. Similar MR behavior has been reported earlier for the B-site doped LSMO system[18, 20]. The MR value increased with Fe concentration to a maximum value of x=0.09%, before decreasing for higher Fe doping concentrations. The MR behavior with Fe doping at Mn site can be explained using a percolation threshold mechanism[40]. The formation of metallic clusters due to Fe doping below the threshold doping concentration enhanced the spin polarized tunneling of the conduction electron thereby increasing MR. The increase in Fe doping above $x \geq 0.9$ increases the localized charge carrier by destroying the ferromagnetic state (Mn^{3+}-O^{2-}-Mn^{3+}) which is responsible for the decrease in MR at higher doping concentrations.

4. Conclusions

The effect of Fe doping on the structural, magnetic and, transport, properties of the $La_{0.7}Sr_{0.3}Mn_{1-x}Fe_xO_3$ (x=0-0.15) has been studied. Structural analysis confirmed the single-phase nature of the Fe-doped LSMO samples prepared, with a small change in lattice parameters due to the similar ionic radii of the Mn and Fe. Chemical analysis confirmed that Fe doping results in an

increase of the Mn^{4+}/Mn^{3+} ratio attributed to Fe^{3+} ions replacing Mn^{3+} in LSMO. Decreased magnetization and increased coercivity of Fe-doped LSMO is described as increased antiferromagnetic super exchange interaction and depletion of ferromagnetic double exchange interaction due to disruption of the long-range ferromagnetic order of Mn ions. The ferromagnetic-paramagnetic transition temperature also decreases with Fe doping due to weakening of the ferromagnetic interaction in the system. The resistivity of the samples increases and T_{MI} decreases with Fe doping concentration due to a depletion of the double exchange mechanism between Mn ions. The MR increased at lower Fe doping concentrations ($x \leq 0.09$), and a maximum value of MR was obtained as 33.8 % at 10 K with a magnetic field of 0.5 T. Above $x \geq 0.09$, a decreased MR due to Fe doping can be explained through the percolation threshold mechanism and was attributed to the localization of the charge carriers. Thus, Fe doping at Mn sites provides an efficient way to improve low field magnetoresistance in the LSMO system for MR based device applications.

Acknowledgment

The authors are thankful to the Science and Engineering Research Board (SERB), New Delhi for providing funding under the grant File Number EMR/2017/000755 for carrying out this work. The authors would also like to thank UGC-DAE, CSR, Indore, and SAIF, IIT-Bombay for providing characterization facilities.

References

1. N. Thorat, K. Shinde, S. Pawar, K. Barick, C. Betty, and R. Ningthoujam, *Dalton Trans.*, **41** (10), 3060-3071 (2012).
2. K. Shinde, S. Pawar, N. Deshpande, J. Kim, Y. Lee, and S. Pawar, *Mater. Chem. Phys.*, **129** (1-2), 180-182 (2011).
3. H. A. Reshi, A. P. Singh, S. Pillai, R. S. Yadav, S. Dhawan, and V. Shelke, *J. Mater. Chem. C*, **3** (4), 820-827 (2015).
4. K. Miyazaki, N. Sugimura, K. Matsuoka, Y. Iriyama, T. Abe, M. Matsuoka, and Z. Ogumi, *J. Power Sources*, **178** (2), 683-686 (2008).
5. A. Molinari, P. M. Leufke, C. Reitz, S. Dasgupta, R. Witte, R. Kruk, and H. Hahn, *Nat. Commun.*, **8** 15339 (2017).
6. A. Sadhu and S. Bhattacharyya, *Chem. Mater.*, **26** (4), 1702-1710 (2014).
7. K. Navin and R. Kurchania, *Appl. Phys. A*, **126** (2), 1-13 (2020).
8. K. Navin and R. Kurchania, *J. Magn. Magn. Mater.*, **448** 228-235 (2018).
9. K. Navin and R. Kurchania, *Ceram. Int.*, **44** (5), 4973-4980 (2018).
10. A. Chen, J.-M. Hu, P. Lu, T. Yang, W. Zhang, L. Li, T. Ahmed, E. Enriquez, M. Weigand, and Q. Su, *Sci. Adv.*, **2** (6), e1600245 (2016).
11. X. Chen, J. Fu, C. Yun, H. Zhao, Y. Yang, H. Du, J. Han, C. Wang, S. Liu, and Y. Zhang, *J. Appl. Phys.*, **116** (10), 103907 (2014).
12. M. Ehsani, P. Kameli, F. Razavi, M. Ghazi, and B. Aslibeiki, *J. Alloys Compd.*, **579** 406-414 (2013).
13. S. Israel, S. S. Kumar, R. Renuretson, R. Sheeba, and R. Saravanan, *Bull. Mater. Sci.*, **35** (1), 107-118 (2012).
14. A. Khare, R. Choudhary, and S. Sanyal, *J. Appl. Phys.*, **112** (2), 023714 (2012).
15. L. Qi, C. Wang, Y. Li, P. Yu, Y. Gao, D. Wu, Y. Yang, Q. Chen, and H. Zhang, *Ceram. Int.*, **47** (5), 5944-5950 (2021).
16. A. D. Souza, S. Rayaprol, A. Sagdeo, A. Sinha, and M. Daivajna, *J. Magn. Magn. Mater.*, **511** 166966 (2020).
17. X. Wang, Q. Chen, L. Li, C. Wang, P. Sun, and H. Zhang, *J. Mater. Sci.: Mater. Electron.*, **30** (20), 19035-19042 (2019).
18. A. Yadav, J. Shah, R. Gupta, A. Shukla, S. Singh, and R. Kotnala, *Ceram. Int.*, **42** (11), 12630-12638 (2016).
19. Y. Zhou, X. Zhu, and S. Li, *Ceram. Int.*, **43** (13), 10026-10031 (2017).
20. Y. Zhou, X. Zhu, and S. Li, *Ceram. Int.*, **43** (4), 3679-3687 (2017).
21. N. Astik, P. K. Jha, and V. Sathe, *Phys. Solid State*, **61** (4), 618-626 (2019).
22. N. M. Astik, H. Soni, P. K. Jha, and V. Sathe, *Physica B: Condens. Matter*, **541** 103-110 (2018).
23. S. Jethva, S. Katba, M. Udeshi, and D. Kuberkar, *Physica B: Condens. Matter*, **520** 13-20 (2017).
24. M. Mootabian, S. R. Ghorbani, A. Kompany, and M. E. Abrishami, *J. Alloys Compd.*, **868** 159185 (2021).
25. L. M. Rodriguez-Martinez and J. P. Attfield, *Phys. Rev. B*, **58** (5), 2426 (1998).
26. N. Kumar, H. Kishan, A. Rao, and V. Awana, *J. Alloys Compd.*, **502** (2), 283-288 (2010).
27. Y. Zhang, T. Phan, D. Yang, and S. Yu, *Curr. Appl. Phys.*, **12** (3), 803-807 (2012).
28. T. Yamashita and P. Hayes, *Appl. Surf. Sci.*, **254** (8), 2441-2449 (2008).
29. T. Zhao, R. Ji, Y. Meng, G. Zhang, H. Si, Y. Wang, M. Yang, F. Wu, L. Li, and R. Chen, *J. Mater. Sci.*, **54** (12), 9098-9110 (2019).
30. M. Nasir, N. Patra, M. A. Ahmed, D. Shukla, S. Kumar, D. Bhattacharya, C. Prajapat, D. Phase, S. Jha, and S. Biring, *RSC Adv.*, **7** (51), 31970-31979 (2017).
31. K. Navin and R. Kurchania, *Ceram. Int.*, **47** (11), 15859-15867 (2021).
32. V. Dayal and S. Keshri, *Solid State Commun.*, **142** (1-2), 63-66 (2007).

33. S. Ogale, R. Shreekala, R. Bathe, S. Date, S. Patil, B. Hannoyer, F. Petit, and G. Marest, *Phys. Rev. B*, **57** (13), 7841 (1998).
34. P. Siwach, P. Srivastava, J. Singh, H. Singh, and O. Srivastava, *J. Alloys Compd.*, **481** (1-2), 17-21 (2009).
35. K. Kubo and N. Ohata, *J. Phys. Soc. Jpn.*, **33** (1), 21-32 (1972).
36. N. Dhahri, A. Dhahri, J. Dhahri, E.-k. Hlil, and E. Dhahri, *J. Magn. Magn. Mater.*, **326** 129-137 (2013).
37. D. Emin and T. Holstein, *Phys. Rev. Lett.*, **36** (6), 323 (1976).
38. N. Mott, *Oxford University Press, Walton Street, Oxford OX 2 6 DP, UK.*, (1987).
39. A. Banerjee, S. Pal, S. Bhattacharya, B. Chaudhuri, and H. Yang, *J. Appl. Phys.*, **91** (8), 5125-5134 (2002).
40. L. Hueso, J. Rivas, F. Rivadulla, and M. López-Quintela, *J. Appl. Phys.*, **89** (3), 1746-1750 (2001).

Figure Captions

Figure.1. Flow diagram of the synthesis process of Fe doped LSMO.

Figure.2. XRD pattern of the Fe doped LSMO samples.

Figure.3. (a) Rietveld refinement of the LSMO and LF15 samples, **(b)** crystal structure of the LSMO, and **(c)** Variation of the crystallite size and cell volume with x (% Fe).

Figure.4. Scanning electron microscopy (SEM), Transmission electron microscopy (TEM) and Energy dispersive spectra and quantitative analysis of **(a)** LSMO**, (b)** LF15 samples, **(c)** EDS maps of the LF15 sample for La, Sr, Mn O and Fe.

Figure.5. X-ray photoelectron spectroscopy (XPS) data of the LSMO, LF6, and LF15 samples **(a)** Survey spectrum **(b)** Mn 2p state, **(c)** Mn^{4+}/Mn^{3+} ratio, and **(d)** Fe 2p state.

Figure.6. M-H data of the Fe doped LSMO at 10 K.

Figure.7. (a) Variation of Saturation magnetization (M_s) and Coercivity (H_c) with Ni concentration, **(b)** M-T measurement of LSMO and LN15

Figure.8. Resistivity with temperature measurement of the Fe doped LSMO samples. Inset shows the fitting of resistivity data by different conduction model.

Figure.9. Variation of resistivity (at T_{MI}) and T_{MI} with Fe doping.

Figure.10. (a) Magnetoresistance (MR) variation with magnetic field at 10K and 300 K, and **(b)** MR variation with Fe concentration at 10K and 300K.

Table Captions

Table-1: Structural parameters obtained from the X-ray diffraction (XRD) data.

Table-2: Magnetic and transport properties of Fe doped LSMO samples.

Table-3: Fitting parameters obtained by fitting the resistivity by different conduction model.

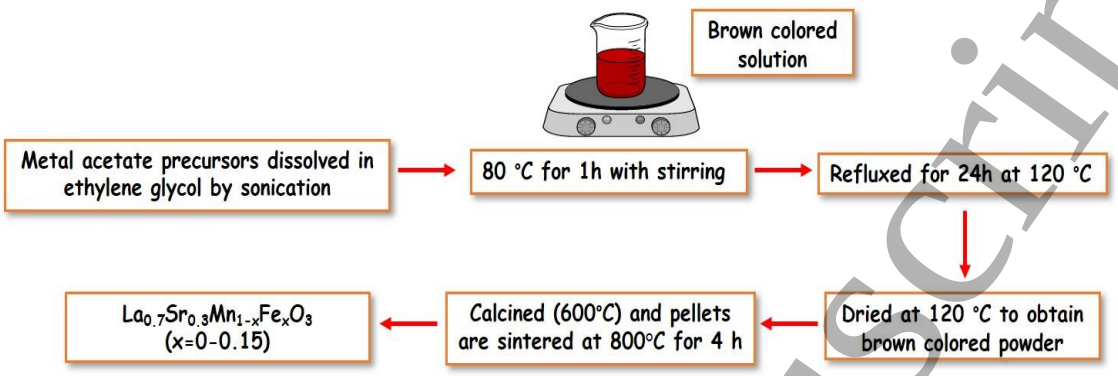

Figure.1. Flow diagram of the synthesis process of Fe doped LSMO.

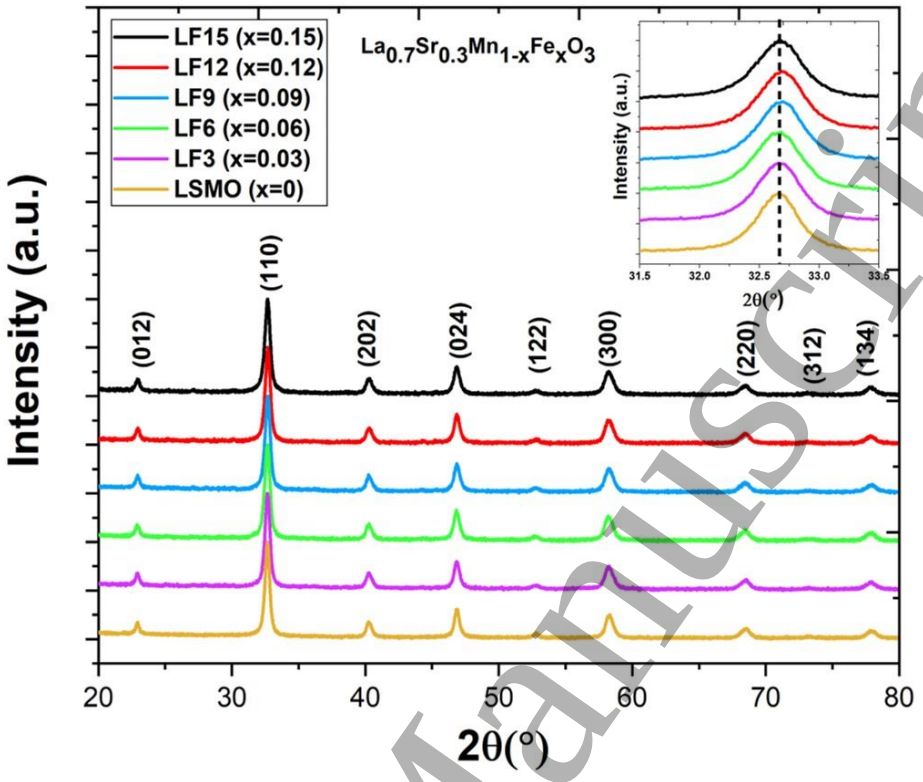

Figure.2. XRD pattern of the Fe doped LSMO samples.

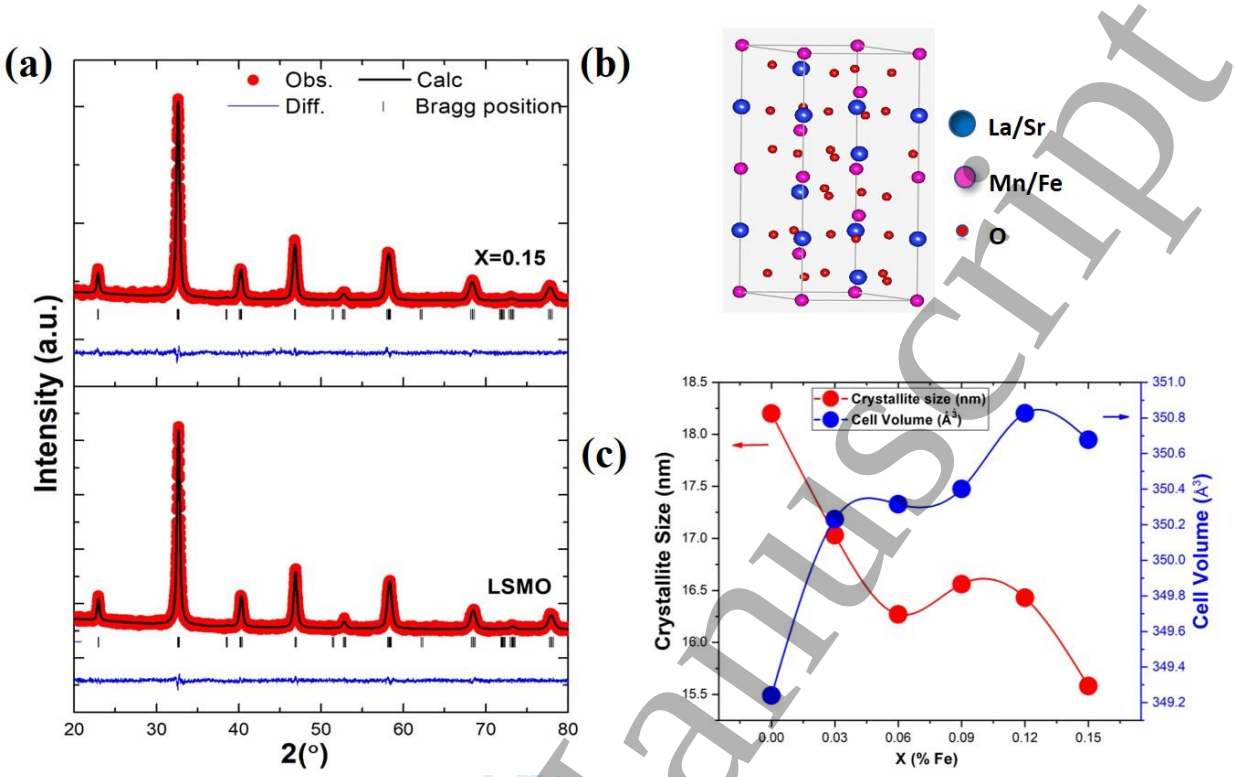

Figure.3. (a) Rietveld refinement of the LSMO and LF15 samples, (b) crystal structure of the LSMO, and (c) Variation of the crystallite size and cell volume with x (% Fe).

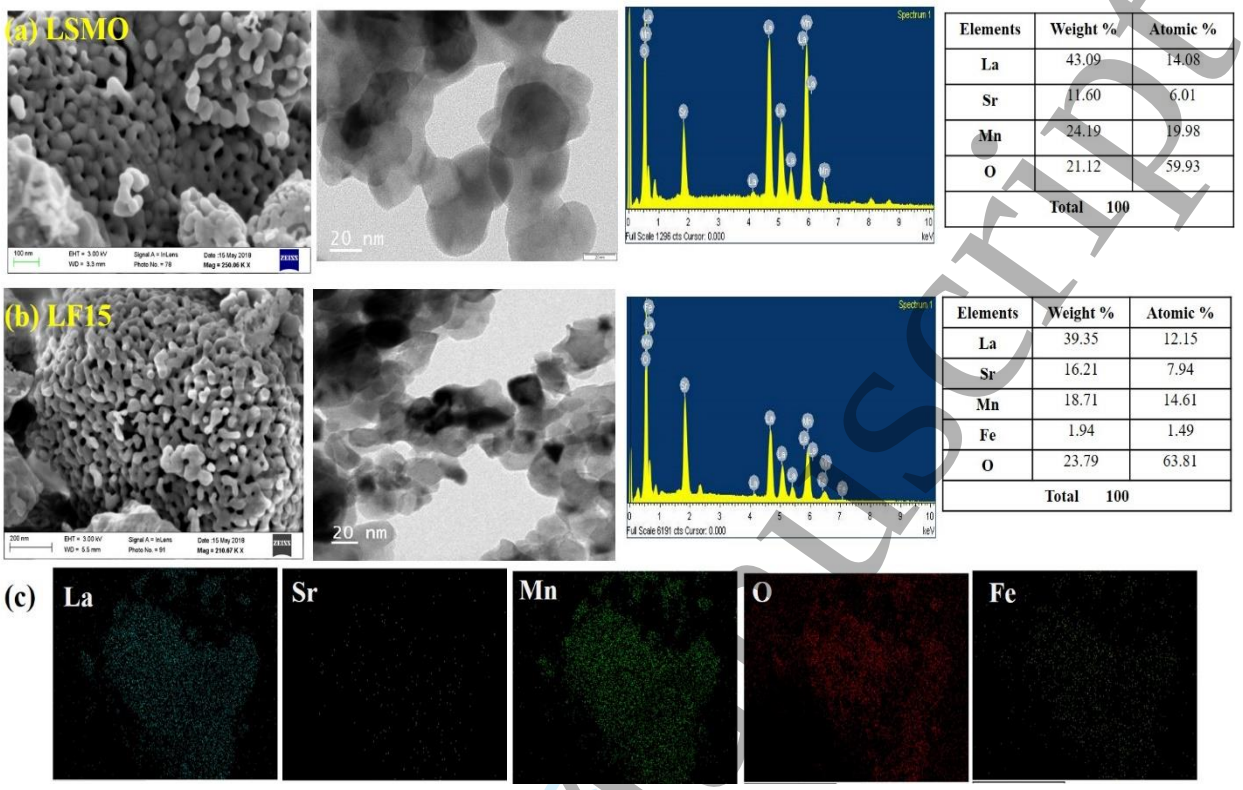

Elements	Weight %	Atomic %
La	43.09	14.08
Sr	11.60	6.01
Mn	24.19	19.98
O	21.12	59.93
Total	100	

Elements	Weight %	Atomic %
La	39.35	12.15
Sr	16.21	7.94
Mn	18.71	14.61
Fe	1.94	1.49
O	23.79	63.81
Total	100	

Figure.4. Scanning electron microscopy (SEM), Transmission electron microscopy (TEM) and Energy dispersive spectra and quantitative analysis of (a) LSMO, (b) LF15 samples, (c) EDS maps of the LF15 sample for La, Sr, Mn O and Fe.

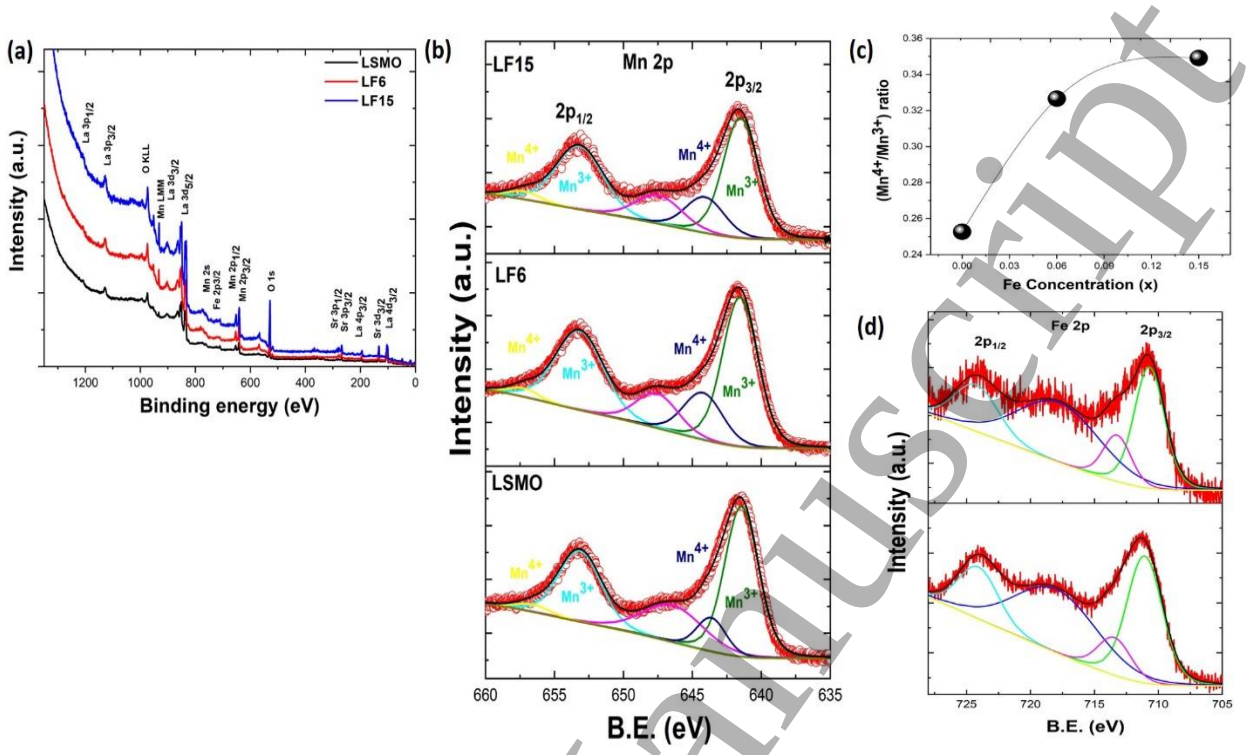

Figure.5. X-ray photoelectron spectroscopy (XPS) data of the LSMO, LF6, and LF15 samples (a) Survey spectrum (b) Mn 2p state, (c) Mn^{4+}/Mn^{3+} ratio, and (d) Fe 2p state.

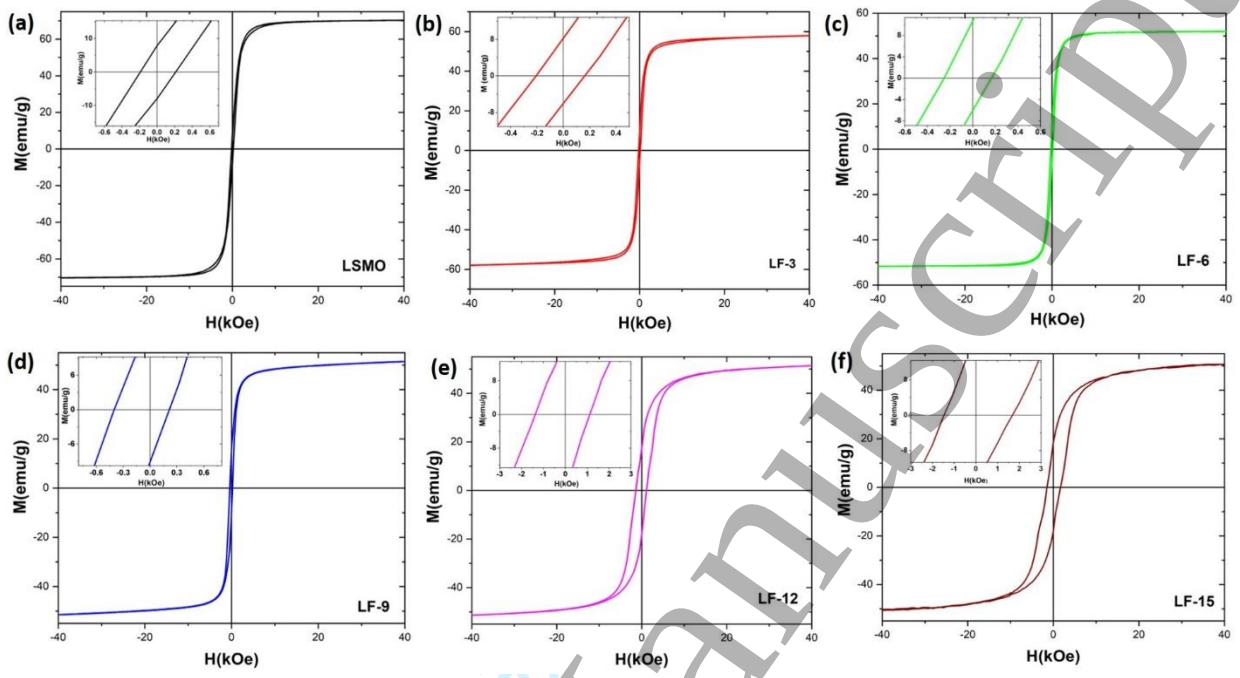

Figure.6. M-H data of the Fe doped LSMO at 10 K.

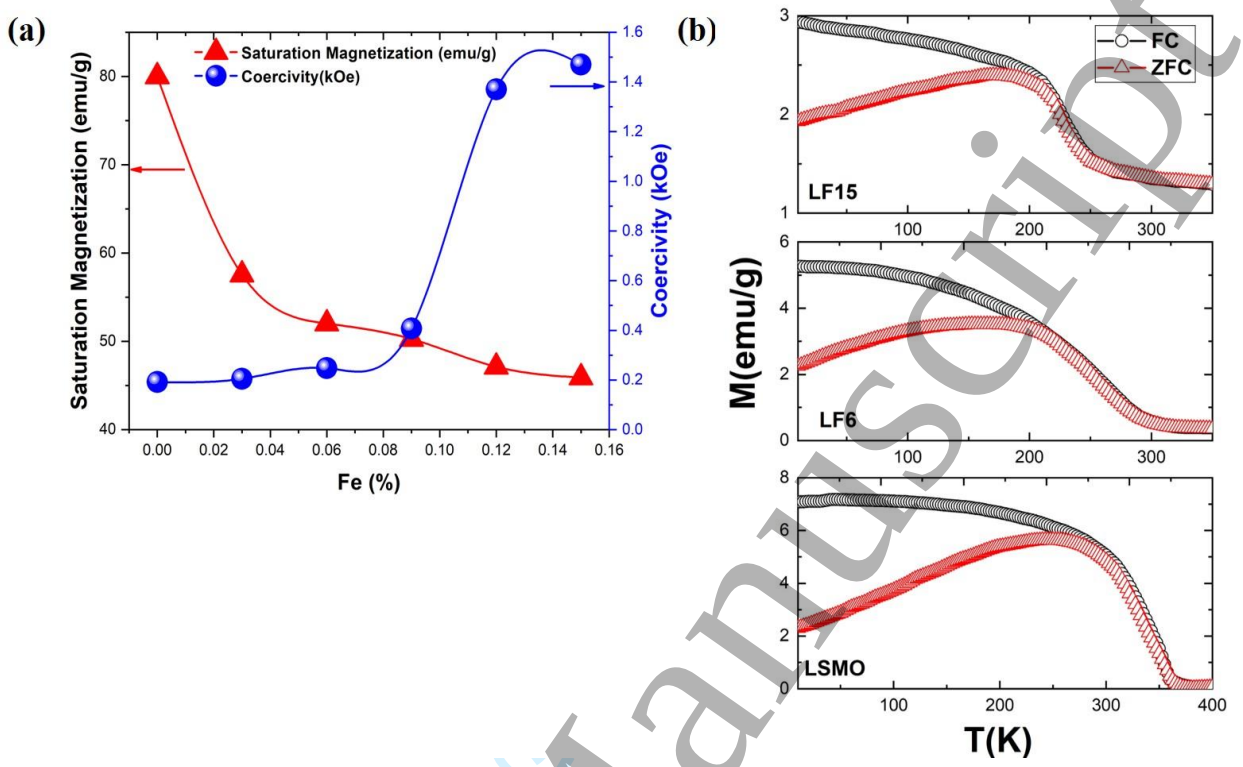

Figure.7. (a) Variation of Saturation magnetization (Ms) and Coercivity (Hc) with Ni concentration, (b) M-T measurement of LSMO and LN15

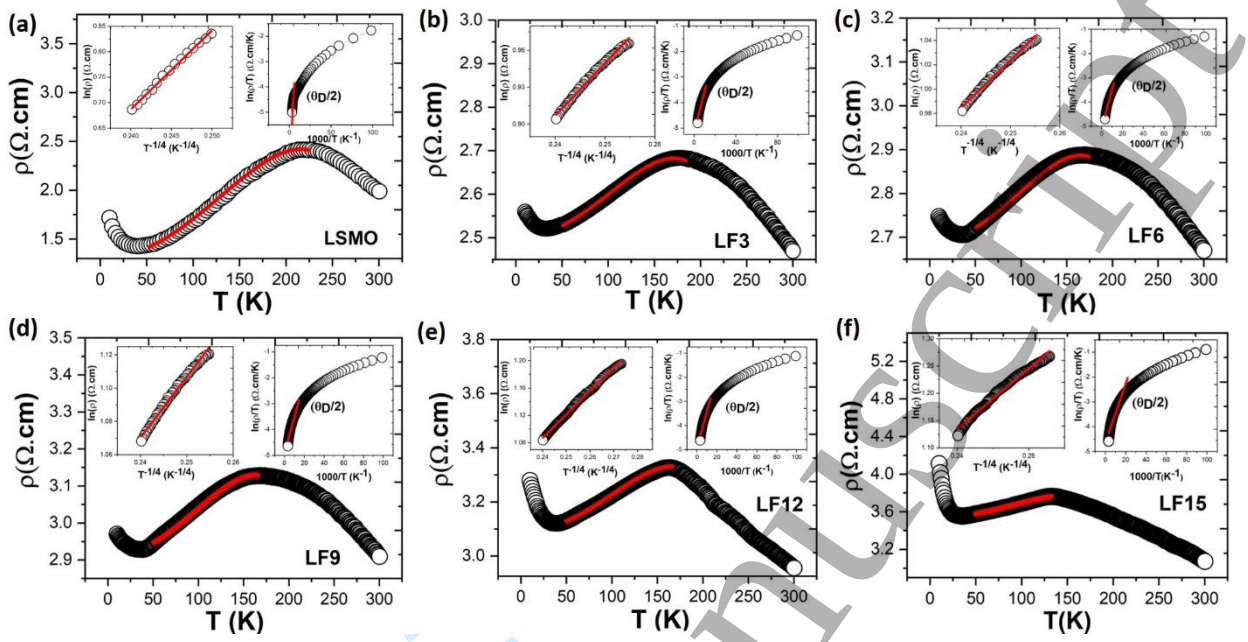

Figure.8. Resistivity with temperature measurement of the Fe doped LSMO samples. Inset shows the fitting of resistivity data by different conduction model.

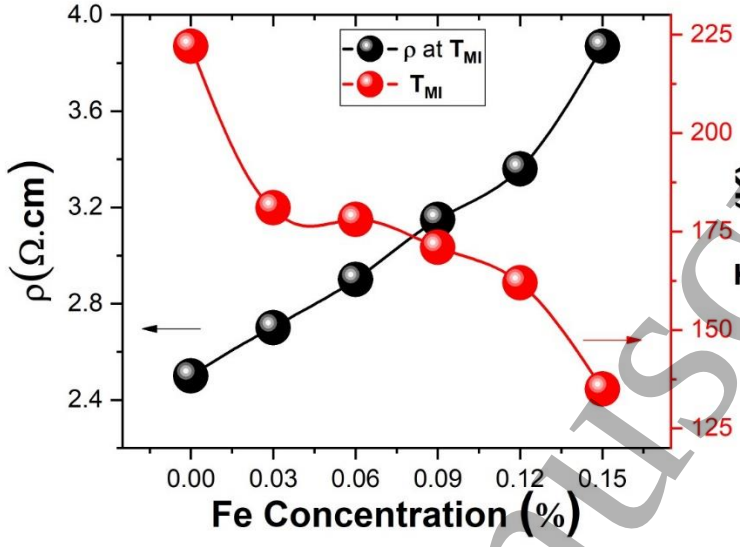

Figure.9. Variation of resistivity (at T_{MI}) and T_{MI} with Fe doping.

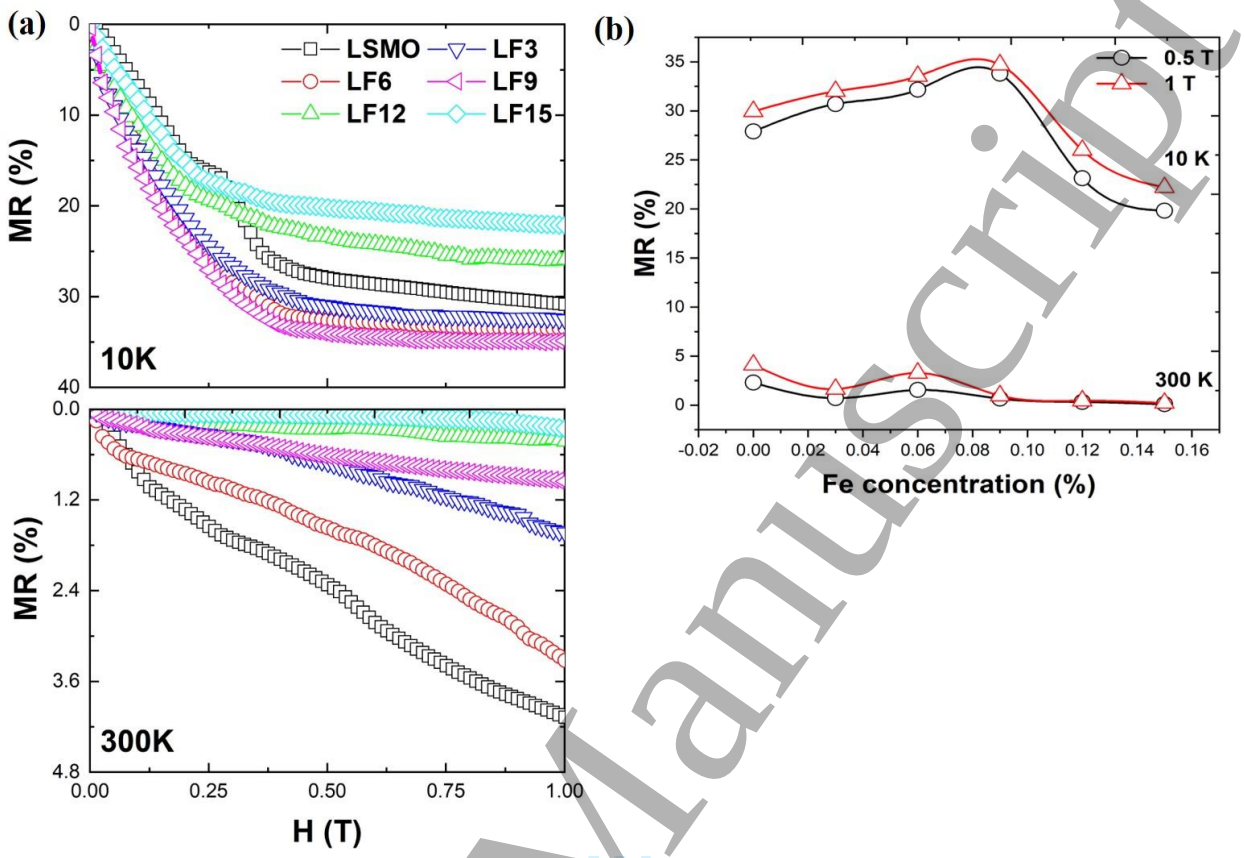

Figure.10. (a) Magnetoresistance (MR) variation with magnetic field at 10K and 300 K, and (b) MR variation with Fe concentration at 10K and 300K.

Table-1: Structural parameters obtained from the X-ray diffraction (XRD) data.

Parameters → / Samples ↓	Crystallite size (nm)	Structure	Lattice parameters (Å)	Cell Volume (Å^3)	Bond length (Å) (Mn-O)	Bond Angle (º) (Mn-O-Mn)
LSMO	18.2	Rhombohedral ($R\bar{3}c$)	a=b=5.4724 c=13.4663	349.247	1.947	168.78
LF3	17.03	Rhombohedral ($R\bar{3}c$)	a=b=5.4767 c=13.4832	350.231	1.952	167.19
LF6	16.27	Rhombohedral ($R\bar{3}c$)	a=b=5.4775 c=13.4824	350.314	1.950	168.38
LF9	16.56	Rhombohedral ($R\bar{3}c$)	a=b=5.4785 c=13.4808	350.401	1.950	168.51
LF12	16.43	Rhombohedral ($R\bar{3}c$)	a=b=5.4820 c=13.4895	350.826	1.951	168.28
LF15	15.58	Rhombohedral ($R\bar{3}c$)	a=b=5.4789 c=13.4893	350.676	1.951	167.87

Table-2: Magnetic and transport properties of Fe doped LSMO samples.

Parameters → / Samples ↓	Saturation magnetization (Ms) (emu/g)	Coercivity (Hc) (kOe)	R (Ω) at T_{MI}	T_{MI} (K)	MR (%) H=0.5 T	
					10K	300K
LSMO	78.5	0.192	2.5	222	27.9	2.3
LF3	57.56	0.205	2.7	181	30.7	0.72
LF6	52.02	0.248	2.9	178	32.1	1.55
LF9	50.27	0.407	3.15	171	33.8	0.67
LF12	47.12	1.370	3.36	162	23.1	0.33
LF15	45.9	1.470	3.87	135	19.8	0.10

Table-3: Fitting parameters obtained by fitting the resistivity by different conduction model.

Parameters → / **Sample** ↓	$\rho=\rho_0+\rho_2T^2+\rho_{4.5}T^{4.5}$			$\rho=\rho_0 exp\ (T_0/T)^{1/4}$		$\rho=\rho_0 T\ exp\ (E_a/k_BT)$	
	ρ_0 ($\Omega.cm$)	ρ_2 ($\Omega.cm\ K^{-2}$) $\times 10^{-4}$	$\rho_{4.5}$ ($\Omega.cm\ K^{-4.5}$) $\times 10^{-10}$	T_0 (K)	$N\ (E_F)$ ($eV^{-1}cm^{-3}$)	θ_D (K)	E_a (meV)
LSMO	1.30	0.432	0.28	5.7×10^4	3.56×10^{22}	342	33.7
LF3	2.5	0.112	0.130	3.32×10^5	6.12×10^{21}	121	43.96
LF6	2.69	0.130	0.165	4.25×10^5	4.77×10^{21}	151.5	45.74
LF9	2.91	0.147	0.19	1.75×10^6	1.16×10^{21}	147.8	48.07
LF12	3.09	0.155	0.19	9.56×10^6	2.12×10^{20}	166	52.95
LF15	3.53	0.198	0.33	1.73×10^7	1.17×10^{20}	110..2	55.23